Aerosol optical properties within the atmospheric boundary layer predicted from ground-based observations compared to Raman lidar retrievals during RITA-2021

Xinya Liu[1], Diego Alves Gouveia[2], Bas Henzing[3], Arnoud Apituley[2], Arjan Hensen[3], Danielle van Dinther[3], Rujin Huang[4], Ulrike Dusek[1]

[1]Centre for Isotope Research (CIO), Energy and Sustainability Research Institute Groningen (ESRIG), University of Groningen, Groningen, 9747 AG, the Netherlands
[2]Royal Netherlands Meteorological Institute (KNMI), De Bilt, 3730 AE, the Netherlands
[3]Department of Climate, Air and Sustainability, TNO, Utrecht, 3584 CB, the Netherlands
[4]State Key Laboratory of Loess and Quaternary Geology, Center for Excellence in Quaternary Science and Global Change, and Key Laboratory of Aerosol Chemistry and Physics, Institute of Earth and Environment, Chinese Academy of Sciences, Xi'an 710061, China

Correspondence to: Ulrike Dusek (u.dusek@rug.nl)

Abstract

In this study, we utilized ground-based in-situ measurements of the aerosol chemical composition and particle size distribution, as well as meteorological data from the Weather Forecasts (ECMWF) to predict vertical profiles of aerosol optical properties, including the aerosol scattering coefficient, backscatter coefficient, extinction coefficient, and lidar ratio. The predicted ambient profiles were compared to retrievals by a multi-wavelength Raman lidar during the Ruisdael Intensive Trace-gas and Aerosol (RITA) campaign in the Netherlands in 2021 for 26 time periods of approximately 1 hour each. Predicted and retrieved extensive aerosol properties (scattering, backscatter and extinction coefficient) were comparable only approximately 35% of the time, mostly under the condition of well-mixed boundary layers. In this case, ground-based measurements can provide a way to extend extinction profiles to lower altitudes, where they cannot be retrieved, as well as to verify the lidar measured profiles. On the other hand, the lidar ratio profiles predicted by ground-based data compared reasonably well to the retrieved lidar profiles (starting at 800 m) also for conditions where the predicted and retrieved backscatter profiles differed considerably. The difference in predicted and retrieved lidar ratio is usually less than ± 30%. Our study thus shows that for well-mixed boundary layers, a representative lidar ratio can be estimated based on ground-based in-situ measurements of dry size distribution and chemical composition taking into account the hygroscopic growth and ambient humidity. This approach offers a method of providing lidar ratios calculated from independent in-situ measurements for simple backscatter lidars or at times, when Raman lidar profiles cannot be measured (e.g. during the day-time). It uses only data that are routinely available at aerosol measurement stations and is therefore not only useful for further validating lidar measurements but also for bridging the gap between in situ measurements and lidar remote sensing.

1   Introduction

Aerosols play an important role in climate change by altering the earth's radiation budget through their interaction with solar radiation. Aerosols reflect part of the sunlight, thereby reducing the radiation at the earth's surface (Twomey, 1977; IPCC, 2013), which results in a cooling effect. On the other hand, certain types of aerosols can also absorb solar radiation, which locally warms the atmosphere and results in a change of the temperature profile, further affecting the atmospheric circulations (Koren et al., 2008; Rosenfeld et al., 2014; Bréon, 2006). In addition, aerosol particles can act as cloud condensation nuclei or ice nuclei affecting the microphysical properties of clouds, and thereby affect the radiation budget indirectly (Graf, 2004; Lohmann and Feichter, 2005; Bréon, 2006). There are still large uncertainties in predicting the contribution of aerosol radiative forcing to climate change, due to the complexity of microphysical and chemical process and their dynamic feedback on the aerosol budget (Kaufman et al., 2005; Feingold, 2001; Graf, 2004). To reduce the uncertainties, observation and simulation of aerosol optical properties and their vertical profiles are essential for a better understanding of aerosol radiative forcing (Moise et al., 2015; Chang et al., 2006).

Light detection and ranging (lidar) is a widely used active remote sensing method for studying the spatial distribution aerosol optical properties (Collis and Russell, 1976; Measures, 1984; Whiteman et al., 1992; Weitkamp, 2005). The detected signal of the elastically backscattered light can be converted into the backscatter and extinction coefficients based on an analytical solution of the so-called "lidar equation" (Klett, 1981; Fernald, 1984) with the assumption of a given extinction to backscatter ratio, called the "lidar ratio". However, the lidar ratio is governed by many factors such as the wavelength of incoming light, the aerosol chemical composition, particle size distribution, relative humidity, and other atmospheric conditions (Salemink et al., 1984; Floutsi et al., 2023). Large errors can occur when retrieving aerosol extinction from backscattered signals. Thus, a Raman lidar technique based on Raman spectroscopy was developed to address this problem (Ansmann et al., 1990). The profiles of the backscatter and the extinction coefficient can be determined independently by the Raman lidar, without the assumption of a lidar ratio (Ansmann et al., 1992a, b). However, a common limitation on the accuracy of the lidar-based retrievals emerges for distances close to the instrument where only a fraction of the atmospheric volume illuminated by the laser pulse is within the lidar's receiver field-of-view, resulting in a "blind zone" at the instrument (no overlap) and a region that is gradually becoming visible for the receiver after some distance (incomplete overlap region) (Wandinger and Ansmann, 2002). While Raman backscatter retrials are less affected by the incomplete overlap region, Raman extinction and elastic lidar retrievals are particularly sensitive to it, even after an overlap correction is applied, and thus it can only accurately record the aerosol profiles above a certain altitude (Hervo et al., 2016; Wandinger and Ansmann, 2002).

Besides active remote sensing, vertical aerosol profiles can also be measured by in situ airborne instruments (Düsing et al., 2021; Haarig et al., 2019; Düsing et al., 2018). These give more accurate information, but are expensive and time consuming and thus lack the temporal coverage of lidar measurements. They are essential in the evaluation of the lidar retrievals and several studies have modelled the aerosol optical vertical profiles based on the Mie theory using the vertically resolved aerosol information but measured by the airborne instruments (Düsing et al., 2021; Ferrero et al., 2019; Düsing et al., 2018). Their

65 results support the usefulness of in situ observations for evaluation of lidar retrievals, however, there are only a few profiles available due to the high cost of the airborne measurements.

In this study, we evaluate a method to predict vertical profiles of the aerosol optical properties using ground-based in situ measurements of the aerosol chemical composition and particle size distribution combined with meteorological profiles from the European Centre for Medium-Range Weather Forecasts (ECMWF). The experiments were performed at Cabauw

70 Experimental Site for Atmospheric Research (CESAR) site in the Netherlands during the Ruisdael land-atmosphere interactions Intensive Trace-gas and Aerosol (RITA) 2021 field campaign[1]. The primary goal of this study is to evaluate if routine ground-based measurements can be used to predict the lidar ratio and the extinction coefficient in the lower atmosphere, where it cannot be retrieved by the Raman lidar. If successful, this information can then be used to extrapolate extinction profiles to the ground or to derive extinction data from elastic backscatter lidars. A further goal is to explore under which

75 circumstances the aerosol measured on the ground can represent the vertical aerosol distribution in the atmosphere. The advantage of the proposed method is that we use only ground-based data that are readily available at most lidar sites and the easily obtained ECMWF data.

2   Methods

2.1   Experiment site and campaign description

80 The RITA campaign was carried out at the CESAR in the Netherlands (51.97◦ N, 4.93◦ E) during Spring (11th May - 24th May) and during Fall (16th September - 12th October) in 2021. CESAR is one of the core observatories for the Ruisdael[2] observatory and also part of the ACTRIS[3] (Aerosol, Clouds and Trace Gases Infra-Structure) and ICOS[4] (Integrated Carbon Observation System). An aerial view of the infrastructure setup during the RITA campaign and the CESAR location are shown in Figure 1. The site is situated in a polder 0.7 m below average sea level and surrounded by a flat pasture landscape. The mode of the

85 wind direction distributions was southwest, but winds were also coming from the northeast, so the potential pollution sources could be from Rotterdam with its large international harbour but also from nearby Utrecht. The ground-based aerosol in situ measurements included the aerosol chemical composition, particle size distribution and aerosol optical properties. The remote sensing observations by the Raman lidar were obtained regularly during the campaign depending on the atmospheric conditions.

---

[1] https://ruisdael-observatory.nl/the-rita-2021-campaign/
[2] https://ruisdael-observatory.nl/ (last access: 20 July 2022)
[3]http://actris.net/ (last access: 20 July 2022)
[4] https://www.icos-cp.eu/ (last access: 20 July 2022)

90
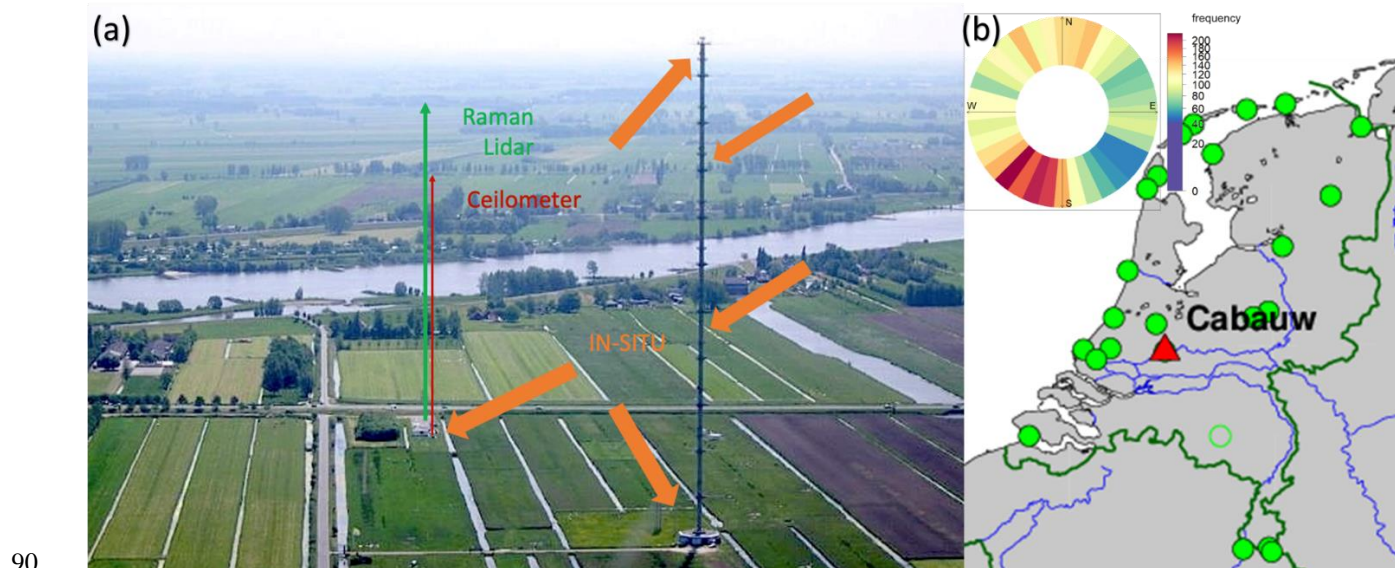
Figure 1: (a) An aerial view of the infrastructure setup during the RITA-2021campaign (photo by Wouter Knap, KNMI). (b) The frequency of the hourly average wind direction at CESAR in RITA campaign from May 7th 2021 to October 20th 2021 and the site (marked in red) location in the Netherlands[5].

2.1.1   Aerosol chemical composition measurements

95   Aerosol chemical composition was measured by different online and offline methods during the campaign.

(i) A time of flight-aerosol chemical species monitor (TOF-ACSM; Aerodyne Research Inc., Billerica, MA) equipped with capture vaporizer (CV) and $PM_{2.5}$ lens measured the mass concentration of non-refractory chemical compounds with a 10-minute time resolution. The TOF-ACSM was installed in a trailer, which was next to the remote sensing site as shown in the Figure 1(a) approximately 200 m distant from the other in situ measurements. The inlet was a Teflon Coated Aluminum

100   cyclone (URG 2000-30ED) with an aerodynamic cut-off diameter of 2.5 µm at ambient conditions and the inlet flow rate was 2.3 L min^{-1} controlled by the ARI Sample Line Flow Controller (S/N FCB-023) at the head of the TOF-ACSM inlet. Particles were dried by a Nafion dryer (Perma Pure, New Jersey). Five chemical species, namely ammonium (NH_4^+), nitrate (NO_3^-), sulphate (SO_4^{2-}), chloride (Cl^-), and organics (Org), were derived based on the fragmentation tables for TOF-ACSM (Fröhlich et al., 2013). The standard calibrations, such as the flow rate calibration, lens calibration and heater bias (HB) voltage tuning

105   were performed before and after the campaign. Ionization efficiency (IE) and the relative ionization efficiency (RIE) were determined by calibration with NH_4NO_3 and $(NH_4)_2SO_4$ solutions with a concentration of 0.005 Mol L^{-1}. The calibration values used in this study are: IE NO_3 = 258.20 pg s^{-1}; RIE NH_4 = 3.51; RIE SO_4 = 1.33; RIE Org =1.40; RIE Chl=1.30; at an air beam (AB) = 4.55E + 5 ions s^{-1}; flow rate = 1.46 cm^3 s^{-1}. The data were processed by the Tofware software (version of 3.2.4, Tofwerk AG, Thun, Switzerland).

---

[5] http://gnss1.tudelft.nl/dpga/station/Cabauw.html

(ii) PM$_{2.5}$ and PM$_{10}$ filter samples were collected for 24 hours using a SEQ47/50 (Leckel GmbH, Germany) instrument with a sequential low-volume system (LVS) of 2.3 m^3 h^{-1} next to the trailer with the TOF-ACSM. The sampler operation was based on the European Standards (EN12341: 1998 and EN14907: 2005). The filter samples were collected under ambient conditions, stored at approximately -20°C, and protected using ice packs during transportation. The concentrations of 3 inorganic anions (NO$_3^-$, Cl$^-$, SO$_4^{2-}$) and 5 cations (Na$^+$, K$^+$, Mg$_2^+$, Ca$_2^+$, NH$_4^+$) were determined by chromatography (ICS-1100, Thermo Scientific). Organic carbon (OC) and elemental carbon (EC) were analysed by a Sunset thermal optical analyzer (TOA, Sunset Laboratory Inc.) using the EUSAAR2 protocol (F. Cavalli, M. Viana, K. E. Yttri, J. Genberg, 2010; Karanasiou et al., 2020). The details of the data evaluation can be found in Liu et al., (2023b).

(iii) the equivalent Black Carbon (eBC) mass concentration was measured by the multi-angle absorption photometer (MAAP model 5012, Thermo Fisher Scientific Inc., Franklin, MA) with 5 minute time resolution (Petzold and Schönlinner, 2004; Petzold et al., 2005). A constant scattering cross section value (6.6 m^2 g^{-1}) based on the user handbook was given for converting the aerosol light absorption coefficient at 670 nm.

The MAAP and the other in situ measurements discussed below were installed in the Cabauw main building, underneath the 213 m high tower as displayed in Figure 1. The MAAP was measuring behind a PM$_{10}$ inlet that was situated 4.5 m above the ground on the roof. A wide diameter Nafion drying system were installed after the PM$_{10}$ size selector to dry the ambient aerosol to an RH below 40%. After the Nafion a manifold split the aerosol flow equally to the multiple instruments.

2.1.2   Particle size distribution measurements

The particle number size distribution (PNSD) was measured by a Scanning Mobility Particle Size Spectrometer (MPSS, TROPOS) and an Aerodynamic particle sizer spectrometer (APS, Model 3321, TSI) which were connected to the same inlet as the MAAP. The MPSS measures particles in the size range from ~10 to 800 nm in electromobility diameter with a time resolution of 5 minutes. Before entering the MPSS, the particles are dried to below 40% relative humidity (RH) by a Perma Pure Nafion air dryer and then charged by a bipolar particle charger (Ni-63). The recorded data was inverted by a custom evaluation software (DMPS-Inversion-2.13.exe) correcting for the diffusion losses of the particles, bipolar charge equilibrium, and the DMA transfer function, as well as the CPC counting efficiency (Wiedensohler et al., 2012). The APS (Peters and Leith, 2003) covers an aerodynamic size range from 0.5 to 20 µm with data recorded in 1-minute time resolution. However, due to the inlet size cut off, the valid size range of the APS is from 0.5 to 10 µm.

The MPSS and APS measured size distributions were merged to create a particle size distribution with a diameter range from 10 nm to 10 µm following the method of Modini et al.(2021). We used the hourly merged particle size distribution to calculate the optical properties for a 5-month period and then compared with the nephelometer measurement. To calculate the vertical profiles, the PNSD data is averaged at a time resolution of 10 minutes. Subsequently, the nearest time period within the radar measurement range is selected for averaging. In this study, the MPSS electrical mobility diameters were assumed to correspond to volume-equivalent diameter, then APS aerodynamic diameters were converted to volume equivalent diameters. However,

shape effects were neglected. The details of joining the PNSD are described in the supplementary material and an example is given in Figure S1.

2.1.3 Ground-based measurements of aerosol optical properties

145 The three-wavelength integrating nephelometer (Dry Neph, TSI Inc., Model 3563) was used to measure the surface aerosol scattering coefficient in a wide angular integration (from 7 to 170°) and the backscatter coefficient (from 90 to 170°) (Anderson et al., 1996; Anderson and Ogren, 1998; Heintzenberg and Charlson, 1996). Scattering coefficients integrated from 0 to 180° were derived based on the truncation correction function proposed in Anderson and Ogren (Anderson and Ogren, 1998). The truncation error ranges from approximately 5% to 10% for submicron particles and from 30% to 50% for particles between 1

150 and 10µm (Anderson and Ogren, 1998; Anderson et al., 1996; Muller et al., 2009). The instrument was located in the main building adjacent to the MAAP and data was collected with a 5-minute time resolution.

2.2 Meteorological observations

The meteorological data used in this study are obtained from the ACTRIS data portal[6], which are the Near Real Time (NRT) data generated by the ECMWF IFS forecast Model with 1-hour time resolution. The RH and temperature profiles derived from

155 the ECMWF model was used in this study. In situ measured meteorological parameters at different heights (7 m, 10 m, 20 m, 40 m, 80 m, 140 m, 200 m) were also recorded cat the 213 m high mast of CESAR tower with a 10-minute time resolution. Data available from May to June in 2021 and can be requested from the KNMI Data Platform[7]. However, we need meteorological profiles that cover the boundary layer depth reaching far beyond the tower height. A radiometer (RPG-HATPRO) located at the CESAR remote sensing site provided vertical profiles of RH and temperature from May to October

160 in 2021. In addition, in-situ measurements of meteorological data were provided by a radiosonde (Vaisala RS92-SGP) carried on a balloon, which was launched every day at around 00:00 UTC from the De Bilt, approximately 25 km from the CESAR site. Previous studies (Fernández et al., 2015; Apituley et al., 2009) concluded that the atmospheric conditions at the CESAR observatory and at the De Bilt site are not significantly different. Therefore, the in-situ measurements from radiosonde were used to evaluate the meteorological profiles during the campaign period. The findings demonstrated that the ECMWF data

165 closely align with the in-situ measurements from the radiosonde by the balloon. Consequently, the ECWMF data was chosen and subsequently utilized in the calculations.

---

[6] https://cloudnet.fmi.fi/ (last access 20 July 2022)
[7] https://dataplatform.knmi.nl(last access: 20 July 2022)

2.3 Remote sensing measurements

2.3.1 CAELI Raman lidar

CAELI is a high power multiwavelength Raman lidar system that is specifically designed for profiling water vapor, aerosols, and clouds (Apituley et al., 2009). CAELI uses a pulsed neodymium-doped yttrium aluminium garnet (Nd:YAG) laser as the light source, emitting laser pulses at 1064 nm (IR), 532 nm (VIS), and 355 nm (UV). The laser and receiver are aligned in a dual-axis configuration with a single target axis pointing vertically to the zenith. The receiving system uses Newtonian telescopes and separate optical channels, with three elastic channels (1064, 532, and 355 nm) and three Raman channels (387 and 607 nm (nitrogen) and 407 nm (water vapor)) to detect the backscattered light signals in the atmosphere. For full tropospheric coverage, CAELI's receiving system is duplicated using a 15 and a 57 cm telescopes for near field range (NFR) and far field range (FFR) measurements respectively. More details on CAELI can be found in Apituley et al. (2009). For this study, the lidar aerosol optical products were retrieved using the EARLINET Single Calculus Chain (SCC) using CAELI's near field telescope measurements and atmospheric model data (D'Amico et al., 2015). To increase signal-to-noise ratio, the raw data vertical resolution was reduced to 60 m and the profiles were usually accumulated for about 1 hour. The Raman backscatter profiles are available starting from 150 m above ground, while the elastic backscatter and Raman extinction coefficient were retrieved above 810 m (overlap function over 97%). To account for the remaining effects of the incomplete overlap above this altitude on the extinction retrievals, an overlap correction was applied based on the method proposed by Wandinger and Ansmann (2002).

2.3.2 CHM15k Ceilometer

The CHM15k ceilometer is a single-wavelength elastic-backscatter lidar manufactured by Lufft (2019), Germany. The CHM15k employs a Nd:YAG narrow-beam microchip laser that emits 1 ns pulses at a wavelength of 1064 nm, with a repetition rate ranging between 5-7 kHz and a receiver field of view of 450 µrad. The laser sensor is capable of measuring heights up to 15 km, with an initial overlap point of 80 m and complete overlap achieved at 800 m above ground (Hervo et al., 2016; Brunamonti et al., 2021). Wiegner and Geiss (2012) reported a relative error of 10% in backscatter coefficient at 1064 nm retrieved through this methodology using a similar system (CHM15kx by Jenoptik, Germany). The data used in this study were processed by the Eumetnet E-PROFILE ALC data hub: https://www.eumetnet.eu/activities/observations-programme/current-activities/e-profile/. The calibrated data with a vertical resolution of 30 m, and a time resolution of 5 minutes can be requested from the KNMI Data Platform (https://dataplatform.knmi.nl/). The ceilometer data was primarily used to aid in the visual discrimination between lofted aerosol layers (possibly from long range transport) and the boundary layer aerosols from recent mixing processes. Figure 2 presents the results of ceilometer measurements from May to October in 2021 with the color scale representing the intensity of the attenuated backscatter signal with the white regions (high intensity) generally correspond to clouds or fog. The orange vertical dashed lines mark the dates on which we conducted the Raman lidar measurements.
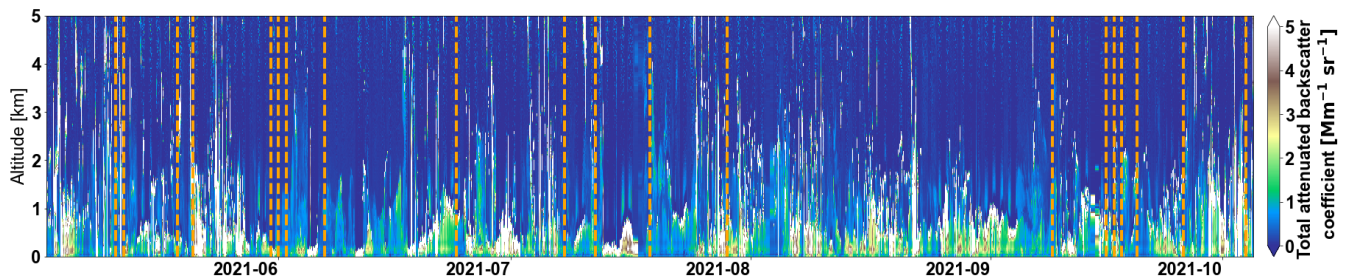
Figure 2: Backscatter coefficient at 1064 nm of CHMk15 ceilometer measurements at CESAR site from May to November in 2021. The orange dash lines represent the CAELI measurements availabilities.

2.4 Calculations
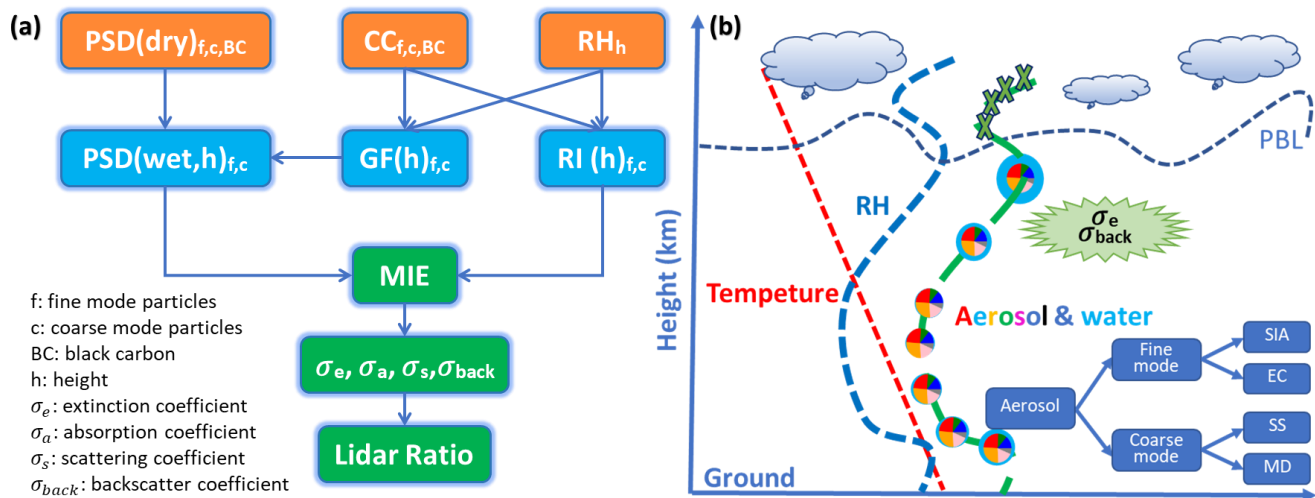
Figure 3: (a) the flow diagram of the calculations, (b) a sketch of the vertical optical properties' calculations.

The aerosol optical properties (including the scattering coefficient, absorption coefficient, extinction coefficient, backscatter coefficient, and lidar ratio) were calculated based on Mie theory as displayed in the Figure 3(a). The main measurement data inputs were: (i) Chemical composition measured by the ACSM and MAAP as described in the section 2.1.1. (ii.) PSD measured by the MPSS and APS as described in the section 2.1.2. (iii.) RH and temperature profiles obtained from the ECMWF as described in the section 2.2.

The PSD was derived by combining data from both the MPSS and the APS, as detailed in Section S1 of the supplementary materials. Starting with the dry aerosol, the PSD data was then separated into fine mode ($< 2.5\,\mu m$) and coarse mode ($> 2.5\mu m$). We assumed that the fine mode was composed of an internal mixture of secondary inorganic aerosol (SIA) including ammonium, nitrate and sulphate, and organics, and that BC was externally mixed. The particle size distribution of BC is derived by multiplying its volumetric proportion within $PM_{2.5}$ by the overall fine particle size distribution. In addition, we assumed that the coarse mode was composed of sea salt (SS) and mineral dust (MD) (Schaap et al., 2010). Because the coarse

mode chemical composition was not measured during the RITA campaign, we employed the average SS and MD fractions obtained from the previous Trolix campaign in 2019[8], which indicated an average composition of 70% SS and 30% MD in volume fraction. The used densities of the SS and MD are listed in Table 1 and calculation details are in the supplementary materials section S3. In addition, we conducted a sensitivity analysis by considering two extreme scenarios: one where the coarse mode was entirely composed of SS and another where it was entirely composed of MD. The outcomes of these sensitivity tests will be elaborated upon in the subsequent discussion. A uniform chemical composition was assumed for fine and coarse mode, respectively.

The refractive index (RI) of the SIA fine mode and the coarse mode was calculated as volume-weighted average of the RI of the individual species (RI_s) (as shown Table 1).

$$RI = \sum_s RI_s \frac{M_s}{\rho_s}, \tag{1}$$

where Ms is the mass concentration of species s and ρ_s is the corresponding density, shown in Table 1. The RI used for BC is given in table 1.

Given the PSDs and the RIs of the dry SIA fine mode, coarse mode and BC, a Mie model (PyMieSca v1.7.5; (Sumlin et al., 2018)) was used to calculate the aerosol optical properties, namely the aerosol scattering coefficient, backscatter coefficient, extinction coefficient and lidar ratio at the wavelengths of the Nephelometer. The calculations were compared to the measured scattering coefficient and backscatter coefficient (see in section 3.1). Sensitivity studies show that the calculations of scattering, backscatter and extinction coefficient are not very sensitive to the assumed BC size distribution.

For the ambient aerosol, a sketch of the calculation for the vertical optical profiles is given in Figure 2(b). In general, we followed the same strategy to separate the aerosols into SIA fine mode and coarse mode and externally mixed BC. A hygroscopic diameter growth factor (GF) is derived for fine (only for SIA because BC was considered as non-hygroscopic) and coarse mode separately. A ambient PSD was calculated by multiplying the dry particle diameters of fine and coarse mode with a diameter GF derived for the respective RH and temperature as a function of different height (j) above ground.

$$PSD_{ambient} = PSD_{dry}GF(S_j), \tag{2}$$

where the GF at each altitude j with given saturation ratio (S_j), is estimated using kappa values (Zhang et al., 2017; Zou et al., 2019; Petters and Kreidenweis, 2007).

$$GF(S_j) = (\frac{K_{mix}S_j}{K_{ej}-S_j} + 1)^{1/3} \tag{3}$$

with

$$K_{ej} = \exp\left(\frac{4\sigma M_w}{RT_j\rho}\right) \tag{4}$$

---

[8] https://ruisdael-observatory.nl/trolix19-tropomi-validation-experiment-2019/

245 where the K_{mix} is the volume weighted average of the individual kappa values of the compound classes listed in the Table S3. For SIA, upper and lower limits (0.5-0.7) were used and accounted for in the uncertainty of the calculated optical properties. K_{ej} depends on temperature T, which varies with altitude. σ is the surface tension of the solution/air interface (here we assume σ = 0.072 J m^{-2}), M_w is the molecular weight of water (M_w = 18 g mol-1), R is the universal gas constant (R = 8.3145 J mol^{-1} k^{-1}), T (K) is temperature, ρ is the density of water (ρ = 1000 kg m^{-3}). This results in two externally mixed, ambient size

250 distributions for the fine mode: black carbon retains the original dry size distribution, and the ambient size distribution of SIA depends on the RH.

Given the GF at height j, the total water volume concentration can be obtained from the difference between the wet integral particle volume size distribution and the dry integral particle volume size distribution based on the following equation:

$$V_{H2Oj} = \sum_i \frac{\pi D_{dryi}^3}{6}(GF_j{}^3 - 1)dn_i, \tag{5}$$

255 where the dn_i is the number concentration (cm^{-3}) of size bin (i) and D_{dry} is the corresponding dry particle diameter (nm). The wet RI for the coarse and the fine mode was calculated as the volume weighted average of the individual RIs of all chemical constituents, now including the calculated water volume concentration in addition to the original volume concentrations. Finally, the optical properties of the ambient aerosol were calculated based on the Mie model with ambient RIs and PSDs as input parameters. The vertical profiles of RIs and PSDs were derived by using the corresponding meteorological profile (RH

260 and temperature) with the assumption of a homogenous distribution of the aerosol within the boundary layer height as sketched in Figure 3(b). The vertical profiles predicted by the model were compared with the Raman lidar measurements in the following section 3.2.

We quantified uncertainties by assessing a set of nine parallel experimental results. These results were obtained by varying two key parameters as mentioned in the previous content: the volume fraction of SS and MD with values of 1, 0.7, and 0; and

265 the SIA kappa values of 0.5, 0.6, and 0.7. The standard deviation of these parallel results serves as calculation uncertainties.

Table 1 The Refractive index, density and kappa values of the chemical composition. The values follow [a] Zou et al. (Zou et al., 2019)**, [b] Düsing et al. (2021), [c] Di Biagio et al. (2019), [d] Bi et al.(2018), Di Biagio et al.(2019), Zieger et al.(2017).**

Chemical composition	RI (refractive index)	Density (g cm-3)	k
SIA	1.53 + 1e-6j	1.75	0.5-0.7
OA	1.47+0.02j[b]	1.40[a]	0.1[b]
BC	1.75+0.55j[b]	1.80[b]	0.0[b]
MD	1.56+0.006j[c]	2.65[e]	0.0[e]
SS	1.5+0.00j[d]	2.07[f]	1.1[f]
H_2O	1.333+0.00j[a]	1.00[a]	-

3   Results and discussion

3.1   Optical properties compared by calculation and Nephelometer at ground level
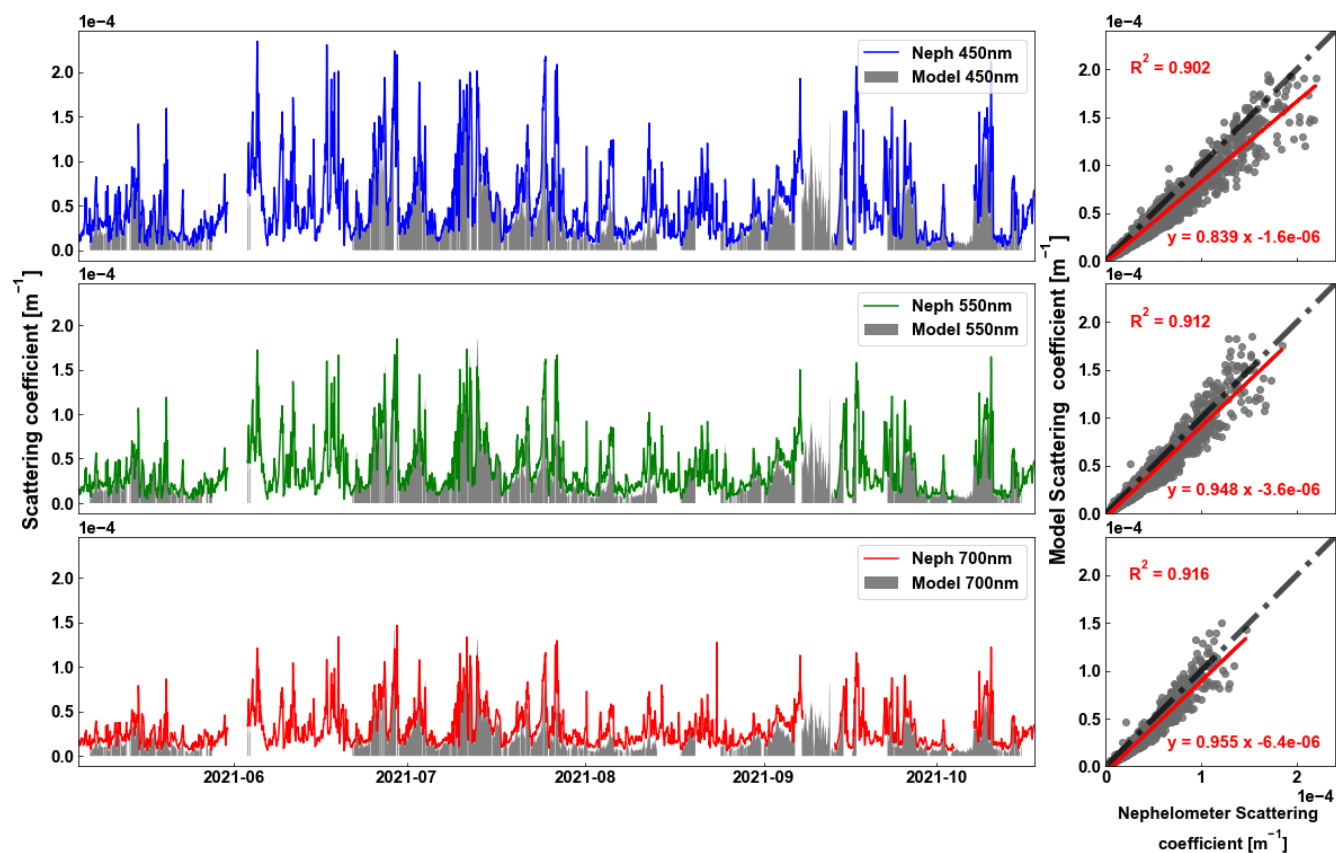
270

Figure 4: Time series of the scattering coefficient at 3 wavelengths (450nm, 550nm 700nm from the top to bottom, respectively) measured by the Nephelometer (coloured lines) and calculated from the Mie model (grey shades) in the left panel; a scatter plot of each wavelength between the measured scattering coefficient (horizontal axis) and the calculated scattering coefficient (vertical axis) in the right panel. The red line represents the regression line, and the black dashed line represents the 1:1 line.
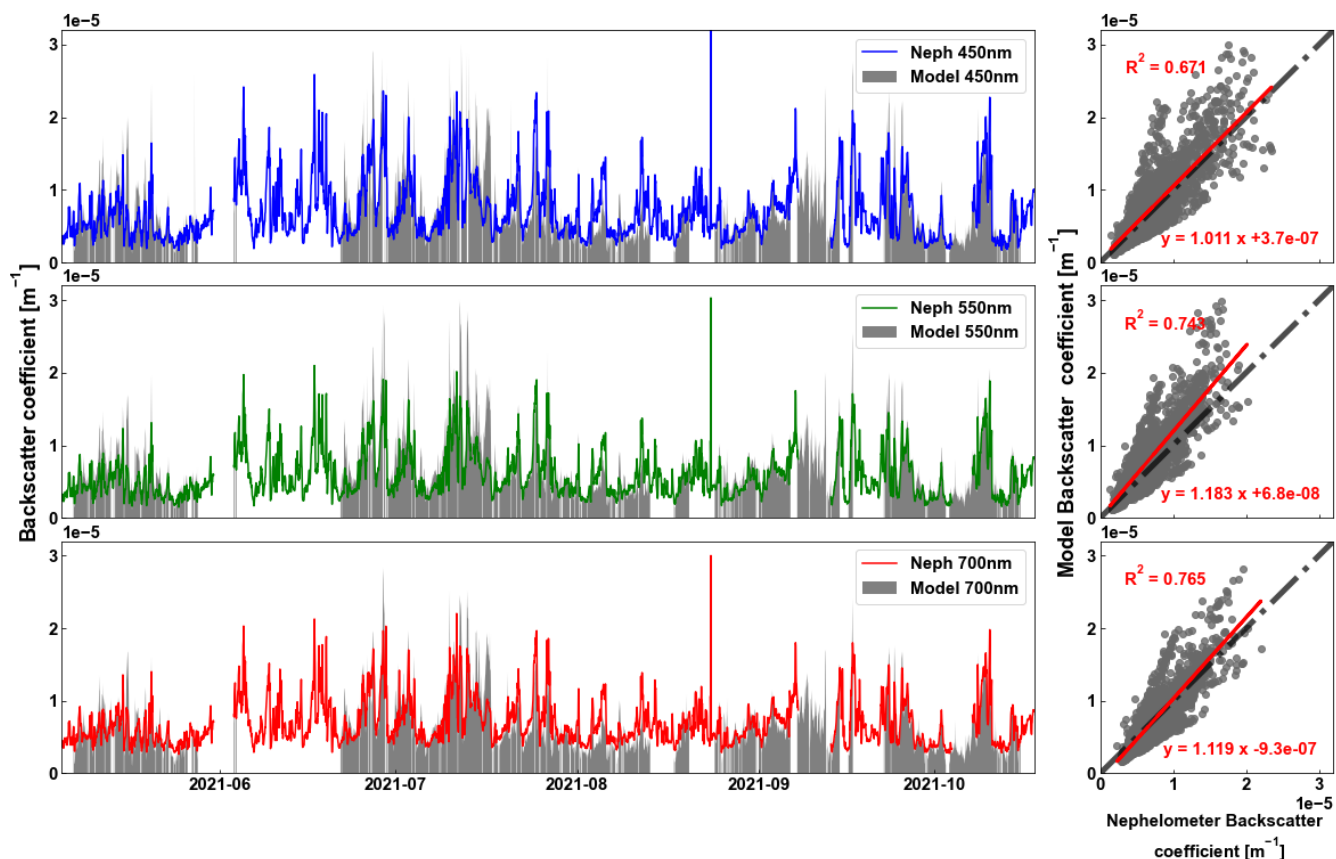
275

Figure 5: Time series of the backscatter coefficient at 3 wavelengths (450nm, 550nm 700nm from the top to bottom, respectively) measured by the Nephelometer (coloured lines) and calculated from the Mie model (grey shades) in the left panel; a scatter plot of each wavelength between the measured backscatter coefficient (horizontal axis) and the calculated scattering coefficient (vertical axis) in the right panel. The red line represents the regression line, and the black dashed line represents the 1:1 line.

280   The Nephelometer (at 450 nm, 550 nm, 700 nm) was operated continuously for measuring the aerosol scattering coefficient and backscatter coefficient at RH below 40%. Data from May to the end of October during the RITA-2021 campaign were used to validate the model calculations. Figure 4 and 5 show the time series of the scattering coefficient and backscatter coefficient at 3 wavelengths obtained by Nephelometer measurements and the calculations outlined in section 2.4. The corresponding scatter plots including best fit lines are given on the right. Gaps in the calculated data are mainly due to

285   maintenance and power failures of the aerosol in situ instruments, but the data coverage is more than 90%. Good agreement was found between the measured and calculated scattering coefficients, with a slope of 0.84 ($R^2 = 0.90$) for 450 nm, and 0.95 ($R^2 = 0.91$) for 550 nm, as well as 0.96 ($R^2 = 0.92$) for 700 nm. The model slightly underestimated the measurements, but the difference becomes smaller at larger wavelengths. Good agreement was also found for the backscatter coefficient, with the slope of the calculated values vs the measured values given as 1.01 ($R^2 = 0.67$) for 450 nm, and 1.18 ($R^2 = 0.74$) for 550 nm,

290   as well as 1.12 ($R^2 = 0.77$) for 700 nm. The model calculations shown in the Figure 4 and Figure 5 assume that the coarse mode is composed of 70% SS and 30% MD as described in section 2.4. Results from a sensitivity study assuming that the coarse

mode consisted either entirely of SS or entirely of MD are presented in Table S1 in the supplementary materials, and are very similar to the results in Figure 4 and Figure 5. More specifically, under the given particle size distribution conditions, the scattering coefficients for these two extreme scenarios differ on average less than 4% across varying wavelengths, the backscatter coefficients less than 19%. This shows that the backscatter coefficient is more sensitive to the coarse mode chemical composition, which can explain the lower R^2 values in Figure 5 compared to Figure 4. However, in general an average chemical composition of the coarse mode for the site is sufficient to predict the optical properties with reasonable accuracy. This is a considerable advantage, as the coarse-mode chemical composition is usually not as readily available as the fine mode composition for many sites. For sites, where the coarse mode comprises a very high mass fraction of PM_{10}, a more accurate representation of the coarse mode chemical composition might be necessary to predict the backscatter coefficient.

3.2   Comparison between the predicted ambient profiles and Raman lidar retrievals

The time periods when the CAELI Raman lidar was operated are marked in Figure 1. Due to unsuitable weather conditions, e.g. shallow atmospheric boundary layer or low clouds layers, it was not possible to retrieve lidar profiles for all time periods. Table S1 summarizes which in-situ data were available on the dates of the Raman lidar measurements. Three representative examples, comprising two polluted cases and one clean case, were selected for detailed discussion in the subsequent section. Additional brief discussions on four more cases are provided in the supplementary materials.

3.2.1 Polluted cases
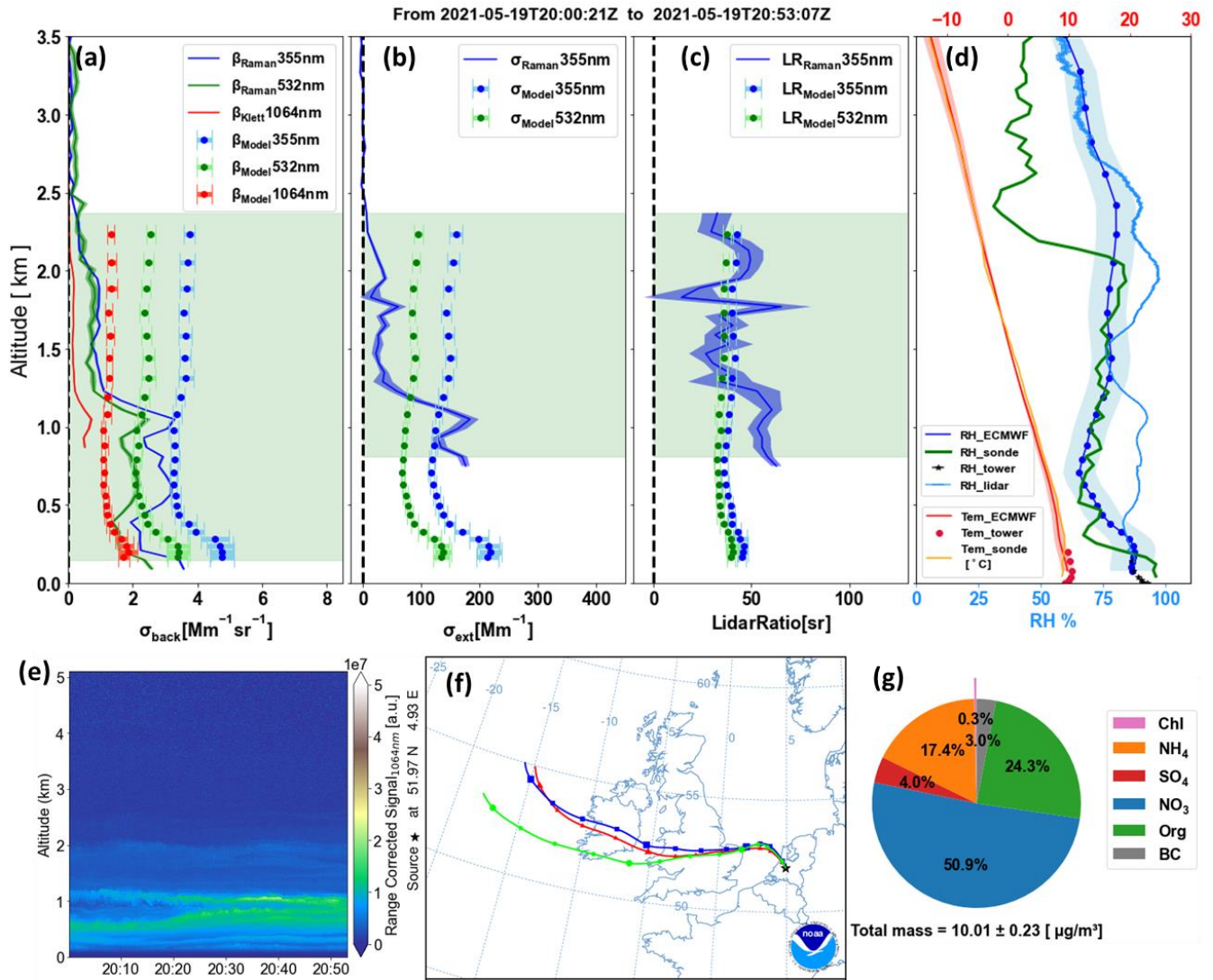
Figure 6: Vertical profiles of the aerosol optical properties (a) the Raman lidar backscatter coefficients (σ_{back}) at 355 nm (blue line), 532 nm (green line), and 1064 nm (using the Klett method; red line). The uncertainties of the measurements are given by the shaded areas. The backscatter coefficient predicted by the Mie calculations at 355 nm (blue dots), 532 nm (green dots), and 1064 nm (red dots) with error bars representing the corresponding uncertainties. (b) the extinction coefficient (σ_{ext}) profiles of the lidar measurements and predictions. (c) the corresponding lidar measured and calculated lidar ratio profiles. The light green background represents upper and lower limits of the valid lidar measurements in plots (a, b and c). (d) The vertical profiles of the RH% and temperature from ECMWF, from Raman lidar, from tower in situ (between 20:00 and 21:00) and Radiosonde (launched from 23:30 to 23:46). (e) The 72 hours back trajectories at 100 (in red), 900 (in blue), 1600 (in green) meters during 20:00 to 21:00. (f) The CAELI Raman lidar Range-corrected signal (RSC) at 1064nm during 20:00 to 20:53. (g) Mass fractions of the chemical composition during 20:00 to 21:00. All data is in UTC time on May-19-2021.

Figure 6 presents the case from 20:00:21 to 20:53:07 (UTC) on May 19, 2021. It includes averaged vertical profiles of aerosol optical properties obtained from Raman lidar retrievals and model calculations, 72-hour backward trajectories from three

altitudes (100 m, 900 m, and 1600 m), the high-resolution Raman lidar measurements at 1064 nm, and the chemical composition from ground measurements. To clarify, the specified time period pertains to the lidar data; for the remaining datasets, the closest time range was selected based on their respective temporal resolutions. In particular, the radiosonde,

325   typically launched once daily around midnight, in this instance recorded a vertical profile from 23:30 to 23:46. Model uncertainties represent the standard deviation across various sensitivity studies as explained in section 2.4. The ECMWF profiles show an uncertainty of 10%. In addition, the valid lidar measurement levels are marked in green background in the Figure 6. The lowest altitude for the backscatter coefficient is above 150 m, whereas the lowest altitude for the extinction coefficient and lidar ratio is 810 m as described in section 2.3.1. Furthermore, the upper limits were manually selected to only

330   include aerosols originating from the planetary boundary layer (including the residual layer, if present) for all the profiles, excluding lofted layers possibly originating from long-range transport. All the subsequent profiles adhered to the same approach. In this case, the dataset spanning from 810 m to 2370 m was employed for subsequent lidar ratio calculations and comparison to the model calculations.

For this study case, the Raman lidar image (Figure 6(e)) shows that, at altitudes below approximately 1000 m, aerosols exhibit

335   layers but they are not distinctly pronounced. Therefore, the lidar retrieved backscatter coefficients (Figure 6(a)) exhibit slight fluctuations in the vertical direction. Between the altitudes of 600 m and 1100 m the retrieved and calculated backscatter coefficients agreed within 12%. Specifically, within this range, the lidar reports values of 2.9 Mm^{-1} sr^{-1} for 355 nm and 2.0 Mm^{-1} sr^{-1} for 532 nm, comparable with calculated values of 3.3 Mm^{-1} sr^{-1} for 355 nm and 2.1 Mm^{-1} sr^{-1} for 532 nm. Below 500 m, the simulated values are higher than the measured values, which is probably partially due to higher values in RH of the

340   ECMWF data compared to the radiosonde measurements in Figure 6(d), but potentially also due to the formation of a stable layer near the ground as shown by an increase of temperature with height in the tower data. Beyond 1100 m, the measured backscatter coefficients rapidly decrease to nearly 0 above the mixed layer and the comparison with ground-based data ceases to be meaningful. This case study demonstrates that ground-based measurements are not very well suited for estimating vertical profiles of extensive aerosol properties (such as the scattering coefficient) under conditions with poor mixing, which often

345   occurs during evening and night-time.

For the extinction coefficient profiles (Figure 6(b)), the Raman lidar retrievals provided good quality data only for 355 nm. A limited overlap existed between the valid lowest retrieved level and the aerosol layer at 1000 m, posing challenges for direct comparisons. The average extinction coefficient at 355 nm, ranging from 800 m to 1200 m, is approximately Mm^{-1} for calculations and slightly higher for retrievals, at about 145 Mm^{-1}.

350   Finally, the retrieved lidar ratio is 45.1 ± 13.7 sr^{-1} at 355 nm for the valid altitudes, whereas the calculations yield a lidar ratio of 40.1 ± 1.6 sr^{-1} at 355 nm and 35.3 ± 1.4 sr^{-1} at 532 nm, as shown in Figure 6(c), showing relatively good agreement between calculations and retrievals. This range of values is typical for a polluted aerosol type (Bohlmann et al., 2018; Groß et al., 2013; Illingworth et al., 2015). The 72-hour back trajectory analysis (Figure 6(f)) at three different altitudes using the Hysplit model (Stein et al., 2015; Rolph et al., 2017) implies that, the air masses originated from the sea, but were transported over Ireland

355   and the United Kingdome and also the northwest of the Netherlands, resulting in elevated levels of anthropogenic pollutants.

This result is in line with ACSM measurements (shown in Figure 6(g)), which indicate an average non-refractory PM$_{2.5}$ mass concentration of 10.01 ± 0.23 µg m^{-3}. Notably, nitrate (50.9%) and ammonium (17.4%) contribute significantly to this mass concentration, which may reflect the substantial contributions from local nitrogen oxides and ammonia emissions to pollution in the Netherlands (Aan de Brugh, 2013).
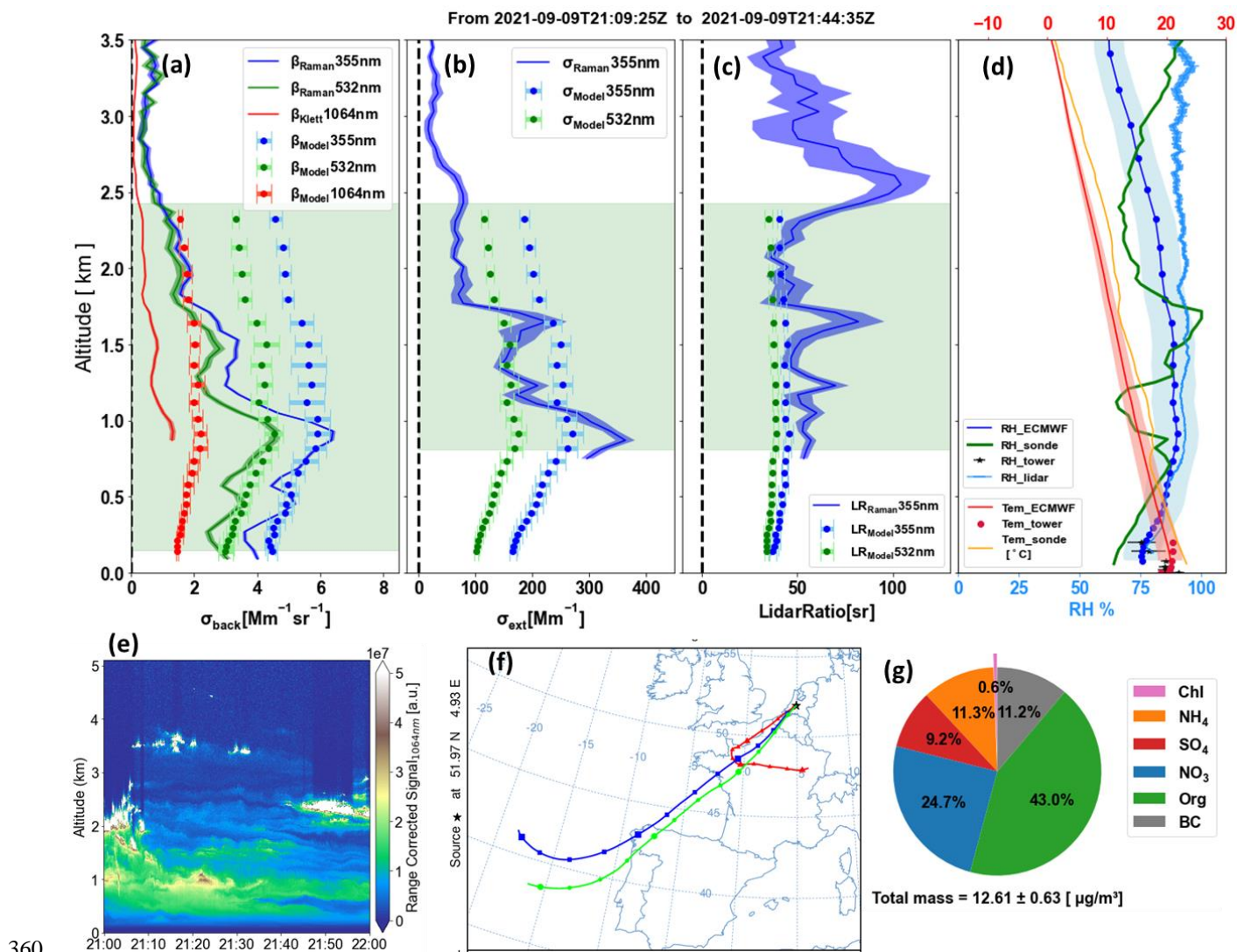
Figure 7: Corresponding to Figure 6 for the period from 21:09:25 to 21:44:35 at UTC time on Sep-09-2021.

Figure 7 shows the second case from 21:09:25 to 21:44:35 (UTC) on Sep-09-2021. The valid retrieval range is from 810 m to 2430 m. The Raman lidar images displayed in Figure 7(f) shows a complex and variable cloud structures before and after this period. The profiles of backscatter coefficients (Figure 7(a)) obtained from Raman lidar retrievals and calculations agree remarkably well from the surface up to an altitude of 1000 m within the mixed layer height. On average, the differences between the two datasets are less than 5% for both 355 nm and 532 nm. Additionally, the backscatter coefficient profiles

increased from the surface to 1000 m, from 3.9 to 6.5 Mm^{-1} Sr^{-1} for 355 nm and from 2.7 to 4.7 Mm^{-1} Sr^{-1} for 532 nm. This increase is reflected in all the RH profiles (from 75% to 90% as displayed in (Figure 7(d)), including those from ECMWF, Raman lidar, tower, and radiosonde (2.5 hours later), which exhibit good consistency. The variations in aerosol optical properties within 1 km altitude were thus primarily due to changes in RH and could be well predicted by ground-based data. However, the ground-based aerosol information is no longer applicable to profiles situated above 1 km.

The extinction coefficient profiles (Figure 7(b)) exhibit higher values initially at around 850 m, followed by a rapid decrease up to an altitude of approximately 1.2 km. The calculated extinction coefficient also decreases above 850 m but much less. This most likely results from a lower aerosol concentration above the mixed layer, particularly during the latter part of the observation period showing in Figure 7(e). Those changes affect the average outcomes of lidar retrievals, resulting in lower values in the extinction profiles. Nevertheless, the extinction profiles of the measurements and calculations at 355 nm agreed reasonably well with a height of about 1 km. Finally, the retrieved and calculated lidar ratios (Fig. 7(c)) are in good agreement throughout the effective column range except around 1.5 km, indicating the presence of similar aerosol types. The lidar average retrievals over the valid retrieval height yielded a value of 53.1 ± 10.8 sr^{-1}, while the model calculations produced a value of 43.2 ± 1.7 sr^{-1} at 355 nm. The analysis of 100m back trajectories, as depicted in Figure 7(f), demonstrated that the air masses originated from Central Europe, while air masses at higher altitudes (900m and 1600m) are shown to originate from the North Atlantic Ocean, and only the last day of the trajectories is very similar for all altitudes. Optical profiles based on ground-level data prove to be effective for altitudes below 900 meters. Compared to the previous polluted case, the ACSM measurements showed a bit higher $PM_{2.5}$ mass concentration of 12.61 ± 0.63 μg m^{-3}, as illustrated in Figure 7(g). The main difference lies in the dominant contribution of organic components (43%).

3.2.2 Clean cases
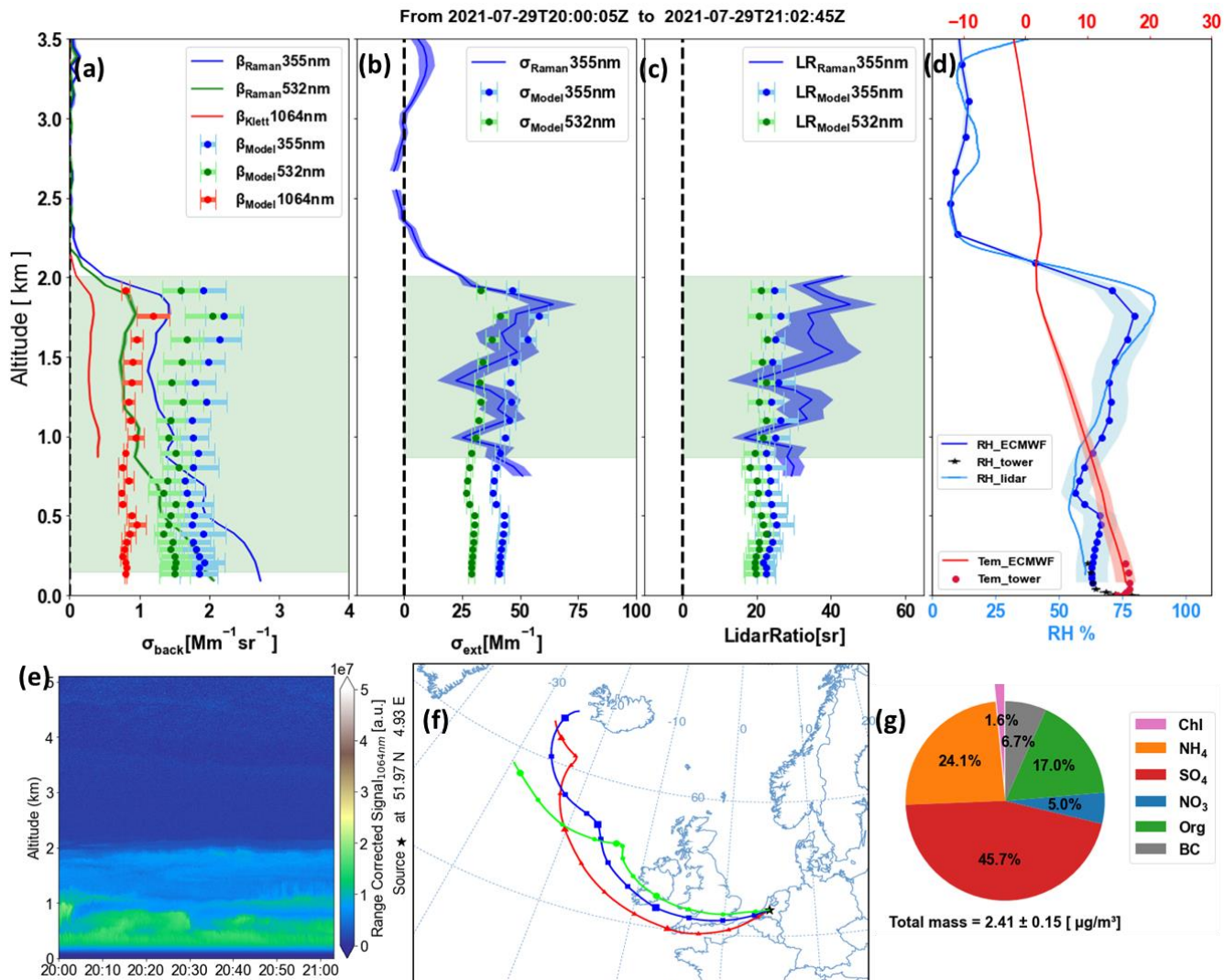
Figure 8: Corresponding to Figure 6 for the period from 20:00:05 to 21:02:45 at UTC time on July-29-2021.

Figure 8 shows the profiles for the period from the 20:00:05 to 21:02:45 (UTC) on July-29-2021. The lidar image (Figure 8(e))

390 reveals two aerosol layers (below 1 km and 1-2 km) during this period, and the applicable range for the extinction profile and lidar ratio spans from 810 m to 2010 m. Figure 8(a) shows that the retrieved backscatter coefficient decreases with altitude, but the calculated backscatter coefficient is rather constant with altitude. The calculations underestimate the retrievals at altitudes below 500 m and overestimate the retrievals (by approximately 20% - 30%) at altitudes around 1500 m. This difference can be attributed to (i) variations in aerosol concentrations or chemical properties between ground-level and higher

395 altitudes; (ii) other inaccuracies in the model such as insufficient information on the size resolved chemical composition and aerosol mixing state; (iii) The RH profiles may be inaccurate, where the 1hr time resolution of the re-analysis data do not

capture correctly the development of a nocturnal stable layer near the ground; As shown in Figure 8(d), below 200m, the RH values from ECMWF and the ground-based tower show good overlap. However, between 200m and 500m, the RH values calculated by the lidar and those from ECMWF by up to 10% RH. Due to the absence of direct measurement data (radiosonde data was unavailable on this day), it is challenging to ascertain which dataset is closer to the actual values. (iv) the lidar retrievals near the ground could also be inaccurate, especially at the low aerosol concentrations in this clean case. However, despite these discrepancies, the calculated values are on the order of magnitude of the retrievals and agree within uncertainties for a large part of the profile.

It is noticeable that the calculated backscatter values have larger uncertainties in this clean case than in the polluted cases. The main reason is that in the clean case the contribution of the coarse more to the backscatter coefficient is larger and thus the extreme assumptions regarding the chemical composition (pure sea salt vs pure mineral dust) starts to affect the results. Since sea salt has a much higher growth factor than mineral dust, the ambient size distribution of the coarse mode differs considerably, especially at high RH. Nevertheless, the resulting uncertainties of the backscatter coefficient are still in a reasonable range.

The agreement between the modelled and retrieved values of extinction coefficient (Figure 8(b)) and lidar ratio profiles (Figure 8(c)) within the altitude range of 800 m to 1800 m suggests a reasonable representation of aerosol properties by the ground-based measurements throughout the boundary layer. Especially, the lidar ratio obtained from the Raman lidar measurements at 355 nm was 31.8 ± 6.8 sr^{-1}, while the model estimated values were 25.0 ± 1.3 sr^{-1} at 355 nm and 21.5 ± 1.1 at 532 nm. These lidar ratios are typical for marine aerosols (around 5 to 30 sr^{-1}) (Bohlmann et al., 2018; Illingworth et al., 2015; Groß et al., 2013). Results are consistent with aerosols originating from marine sources during the observed period, which is supported by the back trajectory shown in Figure 8(f). Additionally, the low aerosol mass concentration (2.41 ± 0.51 µg m^{-3}) shown in Figure 8(g) with a significantly higher fraction of sulphate (45.7%) further supports this result.

All remaining profiles marked in Figure 2 have been stored in a publicly accessible repository (DOI 10.5281/zenodo.11174464), available for interested readers. The results show extinction and backscatter coefficients are sometimes considerably under- or overestimated by the ground-based calculations. However, it is worth emphasizing that the lidar ratios are much better predicted. We speculate that the main reasons for this phenomenon are as follows: (i) the upper-level aerosols may have similar chemical composition and size distribution as surface-level aerosols, but are present at different concentrations. Thus, the backscatter or extinction coefficients of aerosols may be overestimated or underestimated by the same factor, resulting in a similar lidar ratio. (ii) Or it could be the meteorological data may not be sufficiently accurate. Especially when RH is overestimated or underestimated, this has a more significant influence on extinction and backscatter coefficients, but its impact on the lidar ratio is less pronounced. (iii) Another crucial factor may be the influence of shape effects, which normally become more significant for the larger particles. Previous studies show that the backscatter cross-section and extinction cross-section may be underestimated or overestimated by a factor ranging from -2 to +5, depending on the particle shapes and size ranges (Potenza et al., 2016; Geisinger et al., 2017).

 3.3   Summary of the lidar ratio comparison
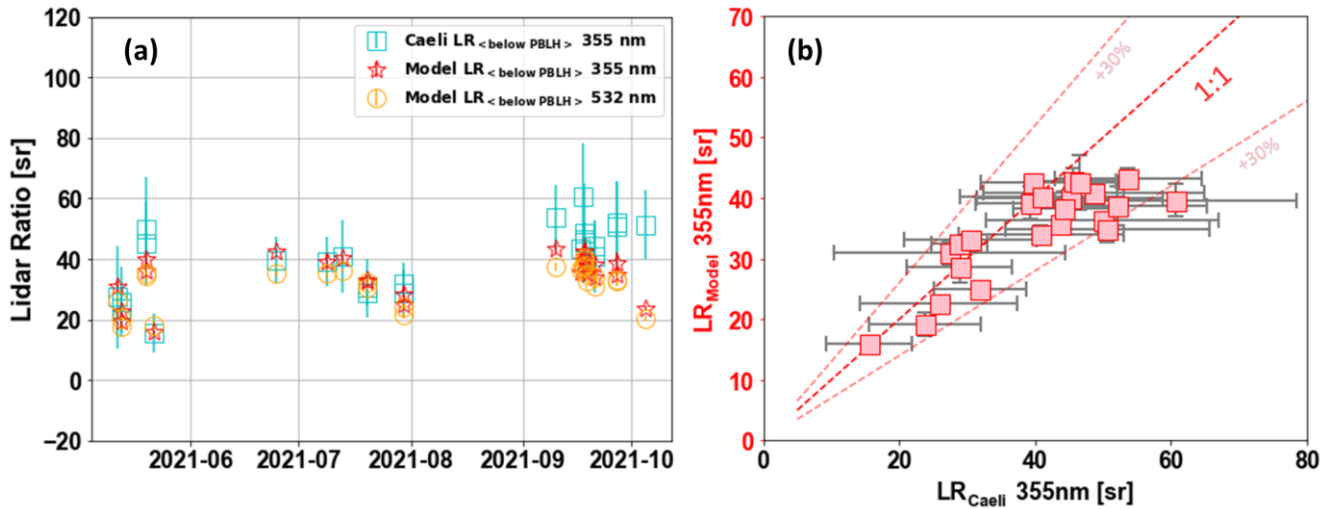
Figure 9: (a) Time series of the mean lidar ratio and its uncertainty (at 355nm and 532 nm) from the valid lidar retrievals and the calculations. (b) Scatter plot of the lidar ratios (LR) from Raman lidar measurements (x axis) and from calculations (y axis) at 355 nm.

435   Figure 9 (a) shows the time series of the average lidar ratios (at 355nm and 532nm) for each period retrieved from lidar measurements and calculated by the model for the corresponding valid retrieval levels of each profile. The error bars correspond to the standard deviation of each effective lidar ratio profile. For the most part, the predicted lidar ratios are comparable to the lidar ratios measured by Raman lidar, however for retrieved lidar ratios above 50 sr, the predictions seem systematically lower. Significant standard deviations in Figure 9 (a) illustrate that the measured lidar ratios were quite variable

440   across the planetary boundary layer, which might indicate different aerosol layers at various altitudes. This cannot be taken into account for the calculations. Consequently, the model-generated lidar ratios tend to remain relatively stable with altitude for the majority of cases. Nevertheless, the predicted lidar ratios are within the range of retrieved lidar ratios, with differences from case to case are usually smaller than $\pm$ 30% for the wavelength at 355nm as shown in Figure 9 (b). On the whole, the calculated lidar ratios were in the range of 16 - 43 sr at 355 nm and 18 - 41 sr at 532 nm on average, indicating a relatively

445   low-pollution environment. Furthermore, the calculations show that the lidar ratio has a small wavelength dependence, with on average higher lidar ratio at 355 nm (slope of 0.64 and R^2 of 0.94 between the lidar ratio at 355 nm and 532 nm). This is consistent with findings from Mattis et al (2004), which summarized a long-term Raman lidar measurements with the lidar ratio from 2000 to 2003 for central European haze, specifically the anthropogenic aerosol particles, with values of 58 ± 12 sr for 355 nm, 53 ± 11 sr for 532 nm, and 45 ± 15 sr for 1064 nm wavelengths in the upper part of the PBL. In the free tropospheric

450   and stratospheric layers, the lidar ratio possibly has a different wavelength dependence, where Moritzet et al. (2004) reported that the lidar ratios were 40 - 45 sr for 355 nm, 65 - 80 sr for 532 nm, and 80 - 95 sr for 1064 nm.

In summary, by integrating data from in situ measurements with the readily accessible ECMWF data, we can predict aerosol optical properties to a certain extent when the aerosol mixing is homogeneous below the boundary layer. Such conditions are

more likely during the day, but occur less often during the evening and night, when Raman lidar data are typically available.

455 While not as sensitive as the retrievals, the calculations are capable of capturing significant shape changes in the vertical distribution. Despite occasional overestimations and underestimations of backscatter and extinction values when assumptions deviate from actual conditions (i.e., homogeneous aerosol mixing), our predictions for the lidar ratio are very effective up to heights of about 2 km. This would allow estimating lidar ratios applicable to simple backscatter lidars from ground-based in-situ measurements. For such calculations, it is crucial for the model to be furnished with an accurate measured particle size

460 distribution including the coarse mode. While possessing chemical insights into the coarse mode is an advantage, it is not absolutely necessary, as long as a typical composition can be assumed. In our case studies, we showed that the extreme assumptions of pure sea salt aerosols vs pure mineral dust aerosols for the coarse mode resulted in reasonable uncertainties in the predicted optical properties for coarse mode mass fractions about 49% on average (range from 14%-81%). This however, does not take into account the uncertainties regarding the shape of pure mineral dust aerosols, which could be considerable.

465 Therefore, in regions dominated by dust aerosols the simple assumption of spherical particle shape might not be appropriate and could result in much larger bias. Within the mixed layer, our results show that the enhancement of the backscatter coefficient and extinction coefficient strongly depend on the particle hygroscopic growth. Consequently, the availability of accurate and high vertical resolution RH profile is important for constructing a robust model input, but even one-hourly ECMWF humidity fields give reasonable results.

470 **4   Conclusions**

In this study, a Mie theory-based model was applied to ground-based in-situ measurements to predict ambient aerosol optical properties including scattering coefficient, backscatter coefficient, extinction coefficient and lidar ratio. The input data are: (i) aerosol chemical composition and (ii) particle size distribution measured at the surface; (iii) the meteorological data from European Centre for Medium-Range Weather Forecasts (ECMWF). The data was collected during the Ruisdael land-

475 atmosphere interactions Intensive Trace-gas and Aerosol (RITA) campaign, at the CESAR site in the Netherlands with a total time span of 5 months (from May to October in 2021). The calculations were first validated by comparing to observations from TSI integrating nephelometer at dry conditions for the entire period. The calculations and measurements across multiple wavelengths with slopes of 0.84 - 0.96 ($R^2 \geq 0.90$) for the scattering coefficients, and slopes of $1.01 - 1.18$ ($R^2 \geq 0.67$) for the backscatter coefficients. Furthermore, the model was compared with aerosol optical vertical profiles retrieved by a multi-

480 wavelength Raman lidar. The results showed that, for a homogeneously distributed aerosol within the mixing layer, the model could effectively simulate the vertical profile of the aerosol backscatter coefficient as a function of RH which varies with altitude. The comparison of extinction coefficients posed challenges due to the limited overlap between the lower layer of retrievals and the mixed layer. However, the profiles at the shared levels exhibited a reasonable connection, suggesting a meaningful comparison could still be made. The simulated lidar ratio can predict the measured lidar ratio within ± 30% for the

485 average values below the planetary boundary layer height. Overall, our study shows that, besides the particle size distribution

and chemical composition, the relativity humidity is a crucial input for the model to generate accurate backscatter and extinction coefficient profiles. Moreover, in the well mixed boundary layer, it is usually possible to approximate the lidar ratio using ground-based measurements. This approach allows for the extension of extinction profiles to lower altitudes that are typically challenging to retrieve, or it can be employed alongside basic backscatter lidar systems to calculate the extinction

490 and then further the aerosol optical depth, which could potentially extend to forecasting aerosol optical depth and could offer advantages in extensive-scale or worldwide radiation simulations.

Data availability

The most data involved in this study is part of the Ruisdael Observatory (https://ruisdael-observatory.nl) project. The ground based measurements can be accessed at repository under https://doi.org/10.5281/zenodo.7924288 (Liu et al., 2023a). The

495 additional model and lidar profiles can be accessed at repository under https://doi.org/10.5281/zenodo.11174465 (Liu et al., 2024). The in situ meteorological data and Ceilometer data are available at the KNMI Data Platform (https://dataplatform.knmi.nl). Other remote sensing data can be accessed from the authors upon reasonable request.

Author contribution

XL, BH, and UD designed this study. DG, AA, AH, DD, UD and XL implemented the experiment and sample analysis. DG

500 and AA provided the lidar retrievals. XL analysed the data and wrote the manuscript. All co-authors proofread and commented on the paper.

Competing interests

The authors declare that they have no conflict of interest.

Acknowledgements

505 The Chinese Scholarship Council (No.201906350118) is acknowledged for the financial support for the author X. Liu. In the project we make use of the Ruisdael observatory infrastructure, funded by the Dutch Science foundation NWO (grant number 184.034.015). The authors thank Delft University of Technology for providing data of the microwave radiometer, which is also an instrument of the Ruisdael Observatory.

References

510 Aan de Brugh, J. M. J.: Aerosol processes relevant for the Netherlands, Chapter 6 pp., 2013.ISBN: 9789461734211

Anderson, T. L. and Ogren, J. A.: Determining Aerosol Radiative Properties Using the TSI 3563 Integrating Nephelometer, Aerosol Sci. Technol., 29, 57–69, https://doi.org/10.1080/02786829808965551, 1998.

Anderson, T. L., Covert, D. S., Marshall, S. F., Laucks, M. L., Charlson, R. J., Waggoner, A. P., Ogren, J. A., Caldow, R., Holm, R. L., Quant, F. R., Sem, G. J., Wiedensohler, A., Ahlquist, N. A., and Bates, T. S.: Performance Characteristics of a High-Sensitivity, Three-Wavelength, Total Scatter/Backscatter Nephelometer, J. Atmos. Ocean. Technol., 13, 967–986, https://doi.org/https://doi.org/10.1175/1520-0426(1996)013<0967:PCOAHS>2.0.CO;2, 1996.

Ansmann, A., Riebesell, M., and Weitkamp, C.: Measurement of atmospheric aerosol extinction profiles with a Raman lidar, Opt. Lett., 15, 746–748, https://doi.org/10.1364/OL.15.000746, 1990.

Ansmann, A., Riebesell, M., Wandinger, U., Weitkamp, C., Voss, E., Lahmann, W., and Michaelis, W.: Combined raman elastic-backscatter LIDAR for vertical profiling of moisture, aerosol extinction, backscatter, and LIDAR ratio, Appl. Phys. B Photophysics Laser Chem., 55, 18–28, https://doi.org/10.1007/BF00348608, 1992a.

Ansmann, A., Wandinger, U., Riebesell, M., Weitkamp, C., and Michaelis, W.: Independent measurement of extinction and backscatter profiles in cirrus clouds by using a combined Raman elastic-backscatter lidar, Appl. Opt., 31, 7113, https://doi.org/10.1364/ao.31.007113, 1992b.

Apituley, A., Wilson, K. M., Potma, C., Volten, H., and Graaf, M. De: Performance Assessment and Application of Caeli — A high-performance Raman lidar for diurnal profiling of Water Vapour , Aerosols and Clouds, 8–11, 2009. https://ruisdael-observatory.nl/cesar-observatory/istp8/data/1753005.pdf

Bi, L., Lin, W., Wang, Z., Tang, X., Zhang, X., and Yi, B.: Optical Modeling of Sea Salt Aerosols: The Effects of Nonsphericity and Inhomogeneity, J. Geophys. Res. Atmos., 123, 543–558, https://doi.org/10.1002/2017JD027869, 2018.

Di Biagio, C., Formenti, P., Balkanski, Y., Caponi, L., Cazaunau, M., Pangui, E., Journet, E., Nowak, S., Andreae, M. O., Kandler, K., Saeed, T., Piketh, S., Seibert, D., Williams, E., and Doussin, J. F.: Complex refractive indices and single-scattering albedo of global dust aerosols in the shortwave spectrum and relationship to size and iron content, Atmos. Chem. Phys., 19, 15503–15531, https://doi.org/10.5194/acp-19-15503-2019, 2019.

Bohlmann, S., Baars, H., Radenz, M., Engelmann, R., and Macke, A.: Ship-borne aerosol profiling with lidar over the Atlantic Ocean: From pure marine conditions to complex dust-smoke mixtures, Atmos. Chem. Phys., 18, 9661–9679, https://doi.org/10.5194/acp-18-9661-2018, 2018.

Bréon, F.-M.: How do aerosols affect cloudiness and climate?, Science (80-.)., 313, 623–624, https://doi.org/10.1126/science.1131625, 2006.

Brunamonti, S., Martucci, G., Romanens, G., Poltera, Y., Wienhold, F. G., Hervo, M., Haefele, A., and Navas-Guzmán, F.: Validation of aerosol backscatter profiles from Raman lidar and ceilometer using balloon-borne measurements, Atmos. Chem. Phys., 21, 2267–2285, https://doi.org/10.5194/acp-21-2267-2021, 2021.

Chang, G. C., Dickey, T., and Lewis, M.: Toward a Global Ocean System for Measurements of Optical Properties Using Remote Sensing and In Situ Observations, Remote Sens. Mar. Environ. Man. Remote Sens., 6, 305–346, 2006. http://opl.ucsb.edu/html-old/tommy/pubs/ChangetalManRemSens06.pdf.

545 Collis, R. T. H. and Russell, P. B.: Lidar measurement of particles and gases by elastic backscattering and differential absorption BT - Laser Monitoring of the Atmosphere, edited by: Hinkley, E. D., Springer Berlin Heidelberg, Berlin, Heidelberg, 71–151, https://doi.org/10.1007/3-540-07743-X_18, 1976.

D'Amico, G., Amodeo, A., Baars, H., Binietoglou, I., Freudenthaler, V., Mattis, I., Wandinger, U., and Pappalardo, G.: EARLINET Single Calculus Chain-overview on methodology and strategy, Atmos. Meas. Tech., 8, 4891–4916, 550 https://doi.org/10.5194/amt-8-4891-2015, 2015.

Düsing, S., Wehner, B., Seifert, P., Ansmann, A., Baars, H., Ditas, F., Henning, S., Ma, N., Poulain, L., Siebert, H., Wiedensohler, A., and MacKe, A.: Helicopter-borne observations of the continental background aerosol in combination with remote sensing and ground-based measurements, Atmos. Chem. Phys., 18, 1263–1290, https://doi.org/10.5194/acp-18-1263-2018, 2018.

555 Düsing, S., Ansmann, A., Baars, H., Corbin, J. C., Denjean, C., Gysel-Beer, M., Müller, T., Poulain, L., Siebert, H., Spindler, G., Tuch, T., Wehner, B., and Wiedensohler, A.: Measurement report: Comparison of airborne, in situ measured, lidar-based, and modeled aerosol optical properties in the central European background -identifying sources of deviations, Atmos. Chem. Phys., 21, 16745–16773, https://doi.org/10.5194/acp-21-16745-2021, 2021.

F. Cavalli, M. Viana, K. E. Yttri, J. Genberg, and J.-P. P.: Toward a standardised thermal-optical protocol for measuring 560 atmospheric organic and elemental carbon: the EUSAAR protocol, https://doi.org/10.1080/00223348708572555, 2010.

Feingold, G., L. A. Remer, J. Ramaprasad, and Y. J. Kaufman (2001), Analysis of smoke impact on clouds in Brazilian biomass burning regions: An extension of Twomey's approach, J. Geophys. Res., 106(D19), 22907–22922, doi:10.1029/2001JD000732.

Fernald, F. G.: Analysis of atmospheric lidar observations: some comments, Appl. Opt., 23, 652–653, 565 https://doi.org/10.1364/AO.23.000652, 1984. https://doi.org/10.1364/AO.23.000652

Fernández, A. J., Apituley, A., Veselovskii, I., Suvorina, A., Henzing, J., Pujadas, M., and Artíñano, B.: Study of aerosol hygroscopic events over the Cabauw experimental site for atmospheric research (CESAR) using the multi-wavelength Raman lidar Caeli, Atmos. Environ., 120, 484–498, https://doi.org/10.1016/j.atmosenv.2015.08.079, 2015.

Ferrero, L., Ritter, C., Cappelletti, D., Moroni, B., Močnik, G., Mazzola, M., Lupi, A., Becagli, S., Traversi, R., Cataldi, M., 570 Neuber, R., Vitale, V., and Bolzacchini, E.: Aerosol optical properties in the Arctic: The role of aerosol chemistry and dust composition in a closure experiment between Lidar and tethered balloon vertical profiles, Sci. Total Environ., 686, 452–467, https://doi.org/10.1016/j.scitotenv.2019.05.399, 2019.

Floutsi, A. A., Baars, H., Engelmann, R., Althausen, D., Ansmann, A., Bohlmann, S., Heese, B., Hofer, J., Kanitz, T., Haarig, M., Ohneiser, K., Radenz, M., Seifert, P., Skupin, A., Yin, Z., Abdullaev, S. F., Komppula, M., Filioglou, M., Giannakaki, E., Stachlewska, I. S., Janicka, L., Bortoli, D., Marinou, E., Amiridis, V., Gialitaki, A., Mamouri, R. E., Barja, B., and Wandinger, U.: DeLiAn - a growing collection of depolarization ratio, lidar ratio and Ångström exponent for different aerosol types and mixtures from ground-based lidar observations, Atmos. Meas. Tech., 16, 2353–2379, https://doi.org/10.5194/amt-16-2353-2023, 2023.

Fröhlich, R., Cubison, M. J., Slowik, J. G., Bukowiecki, N., Prévôt, A. S. H., Baltensperger, U., Schneider, J., Kimmel, J. R., Gonin, M., Rohner, U., Worsnop, D. R., and Jayne, J. T.: The ToF-ACSM: A portable aerosol chemical speciation monitor with TOFMS detection, Atmos. Meas. Tech., 6, 3225–3241, https://doi.org/10.5194/amt-6-3225-2013, 2013.

Geisinger, A., Behrendt, A., Wulfmeyer, V., Strohbach, J., Förstner, J., and Potthast, R.: Development and application of a backscatter lidar forward operator for quantitative validation of aerosol dispersion models and future data assimilation, Atmos. Meas. Tech., 10, 4705–4726, https://doi.org/10.5194/amt-10-4705-2017, 2017.

Graf, H.-F.: The complex interaction of aerosols and clouds, Science (80-.)., 303, 1309–1311, 2004. DOI:10.1126/science.1094411

Groß, S., Esselborn, M., Weinzierl, B., Wirth, M., Fix, A., and Petzold, A.: Aerosol classification by airborne high spectral resolution lidar observations, Atmos. Chem. Phys., 13, 2487–2505, https://doi.org/10.5194/acp-13-2487-2013, 2013.

Haarig, M., Walser, A., Ansmann, A., Dollner, M., Althausen, D., Sauer, D., Farrell, D., and Weinzierl, B.: Profiles of cloud condensation nuclei, dust mass concentration, and ice-nucleating-particle-relevant aerosol properties in the Saharan Air Layer over Barbados from polarization lidar and airborne in situ measurements, Atmos. Chem. Phys., 19, 13773–13788, https://doi.org/10.5194/acp-19-13773-2019, 2019.

Heintzenberg, J. and Charlson, R. J.: Design and applications of the integrating nephelometer: A review, https://doi.org/10.1175/1520-0426(1996)013<0987:DAAOTI>2.0.CO;2, 1996.

Hervo, M., Poltera, Y., and Haefele, A.: An empirical method to correct for temperature-dependent variations in the overlap function of CHM15k ceilometers, 2947–2959, https://doi.org/10.5194/amt-9-2947-2016, 2016.

Illingworth, A. J., Barker, H. W., Beljaars, A., Ceccaldi, M., Chepfer, H., Clerbaux, N., Cole, J., Delanoë, J., Domenech, C., Donovan, D. P., Fukuda, S., Hirakata, M., Hogan, R. J., Huenerbein, A., Kollias, P., Kubota, T., Nakajima, T., Nakajima, T. Y., Nishizawa, T., Ohno, Y., Okamoto, H., Oki, R., Sato, K., Satoh, M., Shephard, M. W., Velázquez-Blázquez, A., Wandinger, U., Wehr, T., and Van Zadelhoff, G. J.: The earthcare satellite : The next step forward in global measurements of clouds, aerosols, precipitation, and radiation, Bull. Am. Meteorol. Soc., 96, 1311–1332, https://doi.org/10.1175/BAMS-D-12-00227.1, 2015.

IPCC, 2013: Climate Change 2013: The Physical Science Basis. Contribution of Working Group I to the Fifth Assessment

Report of the Intergovernmental Panel on Climate Change [Stocker, T.F., D. Qin, G.-K. Plattner, M. Tignor, S.K. Allen, J. Boschung, A. Nauels, Y. Xia, V. Bex and P.M. Midgley (eds.)]. Cambridge University Press, Cambridge, United Kingdom and New York, NY, USA, 1535 pp. https://www.ipcc.ch/report/ar5/wg1/

Karanasiou, A., Panteliadis, P., Perez, N., Minguillón, M. C., Pandolfi, M., Titos, G., Viana, M., Moreno, T., Querol, X., and Alastuey, A.: Evaluation of the Semi-Continuous OCEC analyzer performance with the EUSAAR2 protocol, Sci. Total Environ., 747, https://doi.org/10.1016/j.scitotenv.2020.141266, 2020.

Kaufman, Y. J., Koren, I., Remer, L. A., Rosenfeld, D., and Rudich, Y.: The effect of smoke, dust, and pollution aerosol on shallow cloud development over the Atlantic Ocean, Proc. Natl. Acad. Sci. U. S. A., 102, 11207–11212, https://doi.org/10.1073/pnas.0505191102, 2005.

Klett, J. D.: Stable analytical inversion solution for processing lidar returns, Appl. Opt., 20, 211–220, https://doi.org/10.1364/AO.20.000211, 1981.

Koren, I., Martins, J. V., Remer, L. A., and Afargan, H.: Smoke Invigoration Versus Inhibition of Clouds over the Amazon, Science (80-.)., 321, 946–949, https://doi.org/10.1126/science.1159185, 2008.

Liu, X., Henzing, B., Hensen, A., Dintherand, D. van, and Dusek, U.: Datasets for " Evaluation of the TOF-ACSM-CV for PM1.0 and PM2.5 measurements during the RITA-2021 field campaign," Zenodo, https://doi.org/10.5281/zenodo.7924288, 2023a.

Liu, X., Henzing, B., Hensen, A., Mulder, J., Yao, P., van Dinther, D., van Bronckhorst, J., Huang, R., and Dusek, U.: Measurement report: Evaluation of the TOF-ACSM-CV for PM1.0 and PM2.5 measurements during the RITA-2021 field campaign, Atmos. Chem. Phys., 24, 3405–3420, https://doi.org/10.5194/acp-24-3405-2024, 2024.

Lohmann, U. and Feichter, J.: Global indirect aerosol effects: a review, Atmos. Chem. Phys., 5, 715–737, 2005. https://doi.org/10.5194/acp-5-715-2005

Lufft: User Manual Lufft CHM 15K Ceilometer, 2019. http://ferrarese.bo.isac.cnr.it/~elisabet/sites/default/files/2020-11/Manual_CHM15k_EN_R15_0.pdf

Mattis, I., Ansmann, A., Müller, D., Wandinger, U., and Althausen, D.: Multilayer aerosol observations with dual-wavelength Raman lidar in the framework of EARLINET, J. Geophys. Res. D Atmos., 109, https://doi.org/10.1029/2004JD004600, 2004.

Measures, R. M.: Laser remote sensing: Fundamentals and applications(Book), New York, Wiley-Interscience, 1984, 521 p, 1984.ISBN: 0471081930

Modini, R. L., Corbin, J. C., Brem, B. T., Irwin, M., Bertò, M., Pileci, R. E., Fetfatzis, P., Eleftheriadis, K., Henzing, B., Moerman, M. M., Liu, F., Müller, T., and Gysel-Beer, M.: Detailed characterization of the CAPS single-scattering albedo monitor (CAPS PMssa) as a field-deployable instrument for measuring aerosol light absorption with the extinction-minus-scattering method, Atmos. Meas. Tech., 14, 819–851, https://doi.org/10.5194/amt-14-819-2021, 2021.

Moise, T., Flores, J. M., and Rudich, Y.: Optical Properties of Secondary Organic Aerosols and Their Changes by Chemical Processes, Chem. Rev., 115, 4400–4439, https://doi.org/10.1021/cr5005259, 2015.

Muller, T., Nowak, A., Wiedensohler, A., Sheridan, P., Laborde, M., Covert, D. S., Marinoni, A., Imre, K., Henzing, B., Roger, J. C., Dos Santos, S. M., Wilhelm, R., Wang, Y. Q., and De Leeuw, G.: Angular illumination and truncation of three different integrating nephelometers: Implications for empirical, size-based corrections, Aerosol Sci. Technol., 43, 581–586, https://doi.org/10.1080/02786820902798484, 2009.

Peters, T. M. and Leith, D.: Concentration measurement and counting efficiency of the aerodynamic particle sizer 3321, J. Aerosol Sci., 34, 627–634, https://doi.org/10.1016/S0021-8502(03)00030-2, 2003.

Petters, M. D. and Kreidenweis, S. M.: A single parameter representation of hygroscopic growth and cloud condensation nucleus activity-Part 3: Including surfactant partitioning, Atmos. Chem. Phys., 13, 1081–1091, https://doi.org/10.5194/acp-13-1081-2013, 2007.

Petzold, A. and Schönlinner, M.: Multi-angle absorption photometry—a new method for the measurement of aerosol light absorption and atmospheric black carbon, J. Aerosol Sci., 35, 421–441, https://doi.org/https://doi.org/10.1016/j.jaerosci.2003.09.005, 2004.

Petzold, A., Schloesser, H., Sheridan, P. J., Arnott, W. P., Ogren, J. A., and Virkkula, A.: Evaluation of multiangle absorption photometry for measuring aerosol light absorption, Aerosol Sci. Technol., 39, 40–51, https://doi.org/10.1080/027868290901945, 2005.

Potenza, M. A. C., Albani, S., Delmonte, B., Villa, S., Sanvito, T., Paroli, B., Pullia, A., Baccolo, G., Mahowald, N., and Maggi, V.: Shape and size constraints on dust optical properties from the Dome C ice core, Antarctica, Sci. Rep., 6, 1–9, https://doi.org/10.1038/srep28162, 2016.

Rolph, G., Stein, A., and Stunder, B.: Real-time Environmental Applications and Display sYstem: READY, Environ. Model. Softw., 95, 210–228, https://doi.org/10.1016/j.envsoft.2017.06.025, 2017.

Rosenfeld, D., Sherwood, S., Wood, R., and Donner, L.: Climate effects of aerosol-cloud interactions, Science (80-.)., 343, 379–380, 2014.

Salemink, H. W. M., Schotanus, P., and Bergwerff, J. B.: Quantitative lidar at 532 nm for vertical extinction profiles and the effect of relative humidity, Appl. Phys. B Photophysics Laser Chem., 34, 187–189, https://doi.org/10.1007/BF00697633, 1984.

Schaap, M., Weijers, E. ., Mooibroek, D., Nguyen, L., and Hoogerbrugge, R.: Composition and origin of particulate matter in the Netherlands, RIVM Rapp., 69, 2010. https://www.pbl.nl/sites/default/files/downloads/500099007.pdf

Stein, A. F., Draxler, R. R., Rolph, G. D., Stunder, B. J. B., Cohen, M. D., and Ngan, F.: Noaa's hysplit atmospheric transport and dispersion modeling system, Bull. Am. Meteorol. Soc., 96, 2059–2077, https://doi.org/10.1175/BAMS-D-14-00110.1, 2015.

Sumlin, B. J., Heinson, W. R., and Chakrabarty, R. K.: Retrieving the aerosol complex refractive index using PyMieScatt: A Mie computational package with visualization capabilities, J. Quant. Spectrosc. Radiat. Transf., 205, 127–134, https://doi.org/10.1016/j.jqsrt.2017.10.012, 2018.

670   Twomey, S.: The Influence of Pollution on the Shortwave Albedo of Clouds, J. Atmos. Sci., 34, 1149–1152, https://doi.org/https://doi.org/10.1175/1520-0469(1977)034<1149:TIOPOT>2.0.CO;2, 1977.

Wandinger, U. and Ansmann, A.: Experimental determination of the lidar overlap profile with Raman lidar, Appl. Opt., 41, 511, https://doi.org/10.1364/ao.41.000511, 2002.

Weitkamp, C.: Range-resolved optical remote sensing of the Atmosphere, Springer-Verlag New York, 102, 241–303, 2005.ISBN: 978-0-387-40075-4

675   Whiteman, D. N., Melfi, S. H., and Ferrare, R. A.: Raman lidar system for the measurement of water vapor and aerosols in the Earth's atmosphere, Appl. Opt., 31, 3068–3082, https://doi.org/10.1364/AO.31.003068, 1992.

Wiedensohler, A., Birmili, W., Nowak, A., Sonntag, A., Weinhold, K., Merkel, M., Wehner, B., Tuch, T., Pfeifer, S., Fiebig, M., Fjäraa, A. M., Asmi, E., Sellegri, K., Depuy, R., Venzac, H., Villani, P., Laj, P., Aalto, P., Ogren, J. A., Swietlicki, E., Williams, P., Roldin, P., Quincey, P., Hüglin, C., Fierz-Schmidhauser, R., Gysel, M., Weingartner, E., Riccobono, F., Santos, 680   S., Grüning, C., Faloon, K., Beddows, D., Harrison, R., Monahan, C., Jennings, S. G., O'Dowd, C. D., Marinoni, A., Horn, H. G., Keck, L., Jiang, J., Scheckman, J., McMurry, P. H., Deng, Z., Zhao, C. S., Moerman, M., Henzing, B., De Leeuw, G., Löschau, G., and Bastian, S.: Mobility particle size spectrometers: Harmonization of technical standards and data structure to facilitate high quality long-term observations of atmospheric particle number size distributions, Atmos. Meas. Tech., 5, 657–685, https://doi.org/10.5194/amt-5-657-2012, 2012.

685   Wiegner, M. and Geiß, A.: Aerosol profiling with the Jenoptik ceilometer CHM15kx, Atmos. Meas. Tech., 5, 1953–1964, https://doi.org/10.5194/amt-5-1953-2012, 2012.

Zhang, Z., Shen, Y., Li, Y., Zhu, B., and Yu, X.: Analysis of extinction properties as a function of relative humidity using a κ-EC-Mie model in Nanjing, Atmos. Chem. Phys., 17, 4147–4157, https://doi.org/10.5194/acp-17-4147-2017, 2017.

Zieger, P., Väisänen, O., Corbin, J. C., Partridge, D. G., Bastelberger, S., Mousavi-Fard, M., Rosati, B., Gysel, M., Krieger, 690   U. K., Leck, C., Nenes, A., Riipinen, I., Virtanen, A., and Salter, M. E.: Revising the hygroscopicity of inorganic sea salt particles, Nat. Commun., 8, https://doi.org/10.1038/ncomms15883, 2017.

Zou, J., Yang, S., Hu, B., Liu, Z., Gao, W., Xu, H., Du, C., Wei, J., Ma, Y., Ji, D., and Wang, Y.: A closure study of aerosol optical properties as a function of RH using a K-AMS-BC-Mie model in Beijing, China, Atmos. Environ., 197, 1–13, https://doi.org/10.1016/j.atmosenv.2018.10.015, 2019.

695